ADVANCED MATERIALS
www.advmat.de

An Anode-Free Zn–Graphite Battery

*Gang Wang, Minshen Zhu, Guangbo Chen, Zhe Qu, Benjamin Kohn, Ulrich Scheler, Xingyuan Chu, Yubin Fu, Oliver G. Schmidt, and Xinliang Feng**

The anode-free battery concept is proposed to pursue the aspiration of energy-dense, rechargeable metal batteries, but this has not been achieved with dual-ion batteries. Herein, the first anode-free Zn–graphite battery enabled by efficient Zn plating–stripping onto a silver-coated Cu substrate is demonstrated. The silver coating guides uniform Zn deposition without dendrite formation or side reaction over a wide range of electrolyte concentrations, enabling the construction of anode-free Zn cells. In addition, the graphite cathode operates efficiently under reversible bis(trifluoromethanesulfonyl) imide anion ($TFSI^-$) intercalation without anodic corrosion. An extra high-potential $TFSI^-$ intercalation plateau is recognized at 2.75 V, contributing to the high capacity of graphite cathode. Thanks to efficient Zn plating–stripping and $TFSI^-$ intercalation–deintercalation, an anode-free Zn–graphite dual-ion battery that exhibits impressive cycling stability with 82% capacity retention after 1000 cycles is constructed. At the same time, a specific energy of 79 Wh kg^{-1} based on the mass of cathode and electrolyte is achieved, which is over two times higher than conventional Zn–graphite batteries (<30 Wh kg^{-1}).

1. Introduction

Dual-ion batteries (DIBs) have recently attracted considerable attention due to their high working voltage, low cost, and enormous potential for scalable energy storage applications.[1] The classic cathode used in DIBs is graphitic carbon that works under anion intercalation chemistry.[2] Various anions like PF_6^-, bis(trifluoromethanesulfonyl)imide anion ($TFSI^-$), bis(fluorosulfonyl)imide anion (FSI^-), $AlCl_4^-$, $(BrCl)^{n-}$ have been explored as intercalant species of graphite intercalation compounds (GICs).[3] Owing to the straightforward battery configurations, DIBs have expanded from Li[4] to Na,[5] K,[6] Mg,[7] Ca,[8] and Zn ion[9] systems. Unlike organic or ionic liquid electrolytes, aqueous electrolytes featuring high safety and low cost are experiencing booming development lately.[3f,10] Although significant progress has been made, the key challenge associated with DIBs lies in the low energy density at the device level. Previous attempts to increase the energy density of DIBs mainly rely on using concentrated electrolytes[6,11] to reduce the weight ratio of inactive solvents. However, anodic corrosion on the cathode side can only be suppressed kinetically at ultrahigh concentrations. It remains a stability concern when the majority of electrolytes is consumed during DIB charging. The plating–stripping efficiency of the metal anode also depends strongly on the passivation interphase formed under the concentrated electrolyte. In the previous DIB prototypes, an excess of the metal anode and electrolyte was always required.

Recently, the "anode-free" Li-metal battery concept has been developed using an inactive substrate as the current collector,[12] which is much safer and more convenient than Li metal both

G. Wang, G. Chen, X. Chu, Y. Fu, X. Feng
Center for Advancing Electronics Dresden & Department of Chemistry and Food Chemistry
Technische Universität Dresden
01062 Dresden, Germany
E-mail: xinliang.feng@tu-dresden.de

G. Wang, X. Feng
Department of Synthetic Materials and Functional Devices
Max Planck Institute for Microstructure Physics
D-06120 Halle (Saale), Germany

The ORCID identification number(s) for the author(s) of this article can be found under https://doi.org/10.1002/adma.202201957.

DOI: 10.1002/adma.202201957

M. Zhu, Z. Qu, O. G. Schmidt
Center for Materials
Architectures, and Integration of Nanomembranes
TU Chemnitz
09126 Chemnitz, Germany

M. Zhu, Z. Qu, O. G. Schmidt
Material Systems for Nanoelectronics
TU Chemnitz
09107 Chemnitz, Germany

B. Kohn, U. Scheler
Leibniz-Institut für Polymerforschung Dresden e.V.
01069 Dresden, Germany

O. G. Schmidt
School of Science
TU Dresden
01062 Dresden, Germany

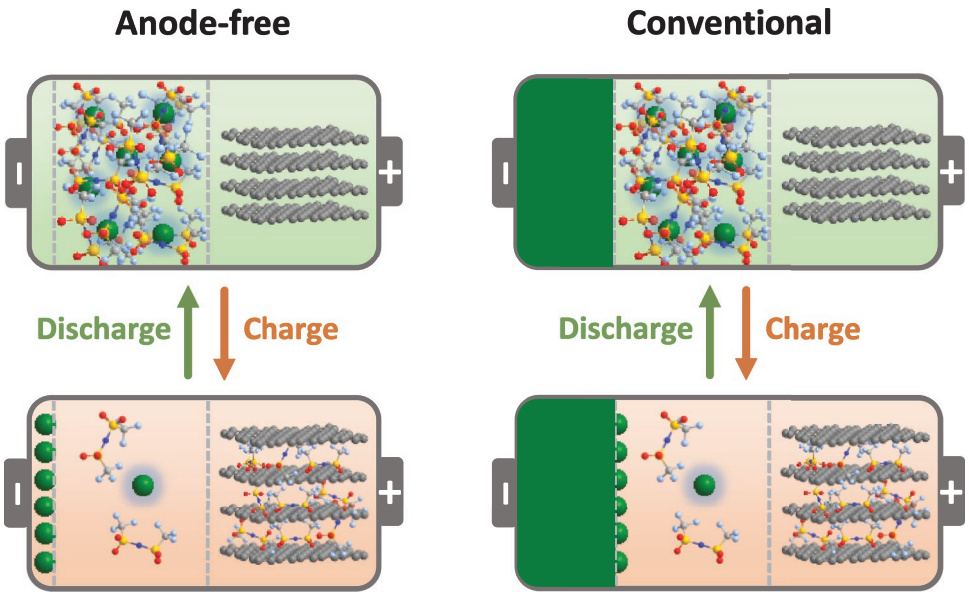

Scheme 1. Working principle of the "anode-free" ZGB and comparison with conventional ZGB.

in warehousing and during cell assembly from a practical perspective. More importantly, in this configuration, Li metal will be deposited onto the substrate during charge to replace Li^+ host graphite in commercial Li-ion batteries, therefore, much battery weight (≈30%) can be saved to achieve high energy density. An "anode-free" Na battery[13] was reported via guiding Na deposition onto the carbon nucleation layer. "Anode-free" Zn batteries[14] were also accomplished recently in water-based electrolytes. However, such an "anode-free" configuration has not been realized in DIBs due to unsatisfactory anode metal plating–stripping efficiency and/or narrow potential window of existing electrolytes.

Herein we demonstrate the first "anode-free" DIB in the Zn-ion system. The constructed "anode-free" Zn–graphite battery (ZGB) comprises an anode substrate, a graphite cathode, and $Zn(TFSI)_2$/ethyl methyl carbonate (EMC) electrolyte (**Scheme 1**). The applied anode substrate is Cu foil with a thin layer (40 nm) of silver (Ag) coating. The Ag coating directs uniform deposition of Zn on the anode side without dendrite or side reaction, achieving 99.90% plating–stripping Coulombic efficiency (CE) within only two cycles in both dilute and concentrated electrolytes. The graphite cathode works efficiently in $Zn(TFSI)_2$/EMC electrolyte with a new high-potential intercalation plateau observed at 2.75 V (vs Zn^{2+}/Zn). As a result, the assembled "anode-free" ZGB performs well in long-term cycling (1000 cycles) with 82% capacity retention and outputs specific energy of 79 Wh kg^{-1} based on the mass of cathode and electrolyte, which is much higher than those (<30 Wh kg^{-1}) of conventional ZGBs.

2. Results and Discussion

2.1. Electrolyte Property

The property of electrolyte, which functions as the active salt reservoir of DIBs, plays a significant role in the operation of "anode-free" ZGB. A 3 *m* $Zn(TFSI)_2$/EMC electrolyte was prepared by dissolving 1.88 g $Zn(TFSI)_2$ (3 mmol) into 1 mL EMC, producing a transparent solution (**Figure 1**a). Other electrolytes with different concentrations were prepared as well by adjusting the amount of $Zn(TFSI)_2$. The concentration unit (*m*) used here is defined as 1 mmol salt dissolved into 1 mL solvent for operation convenience, which is distinct from molar concentration (M). The ionic conductivity of $Zn(TFSI)_2$/EMC electrolyte varies as a function of concentration, with a maximum value (8.3 mS cm^{-1}) achieved at 1 *m* (Figure 1b). Increasing the concentration from 1 *m* to 3 *m* results in the decline of ionic conductivity (to 1.1 mS cm^{-1}) due to viscosity enhancement, while the Zn transference number rises from 0.335 to 0.564 (Figure 1c and Figure S1, Supporting Information). This result indicates that Zn^{2+} slightly dominates the ion diffusion within the concentrated electrolyte, and the diffusion of large $TFSI^-$ is controlled by concentration to a greater extent. The concentration influence of electrolyte on anion diffusion was further analyzed by diffusion nuclear magnetic resonance (NMR) measurements (Figure 1d). ^{19}F and ^1H were utilized for $TFSI^-$ diffusion and solvent self-diffusion, respectively. Increasing the electrolyte concentration from 0.001 to 3 *m* slows down the diffusion coefficients by two orders of magnitude for both EMC solvent and $TFSI^-$. No dependence of the diffusion coefficient was observed on the diffusion time. The concentration of $Zn(TFSI)_2$/EMC electrolyte could be further enhanced at the expense of a lower ionic conductivity (0.26 mS cm^{-1} for 4 *m* $Zn(TFSI)_2$/EMC) and an undetermined Zn transference number, which prevented smooth Zn plating–stripping and stable operation of ZGB (discussed in the following sections). To balance the ionic conductivity, diffusion of Zn^{2+} and $TFSI^-$, and to maximize the weight ratio of active salt, 3 *m* was expected as a suitable concentration of $Zn(TFSI)_2$/EMC electrolyte in this study.

In consideration of the high working potential of graphite cathode, the cathode substrate has to withstand the corrosive $TFSI^-$[9a] at high potential and ensure $Zn(TFSI)_2$/EMC electrolyte with a wide electrochemical stability window. Because of the excellent anti-corrosion feature of tungsten (W),[15] we identified

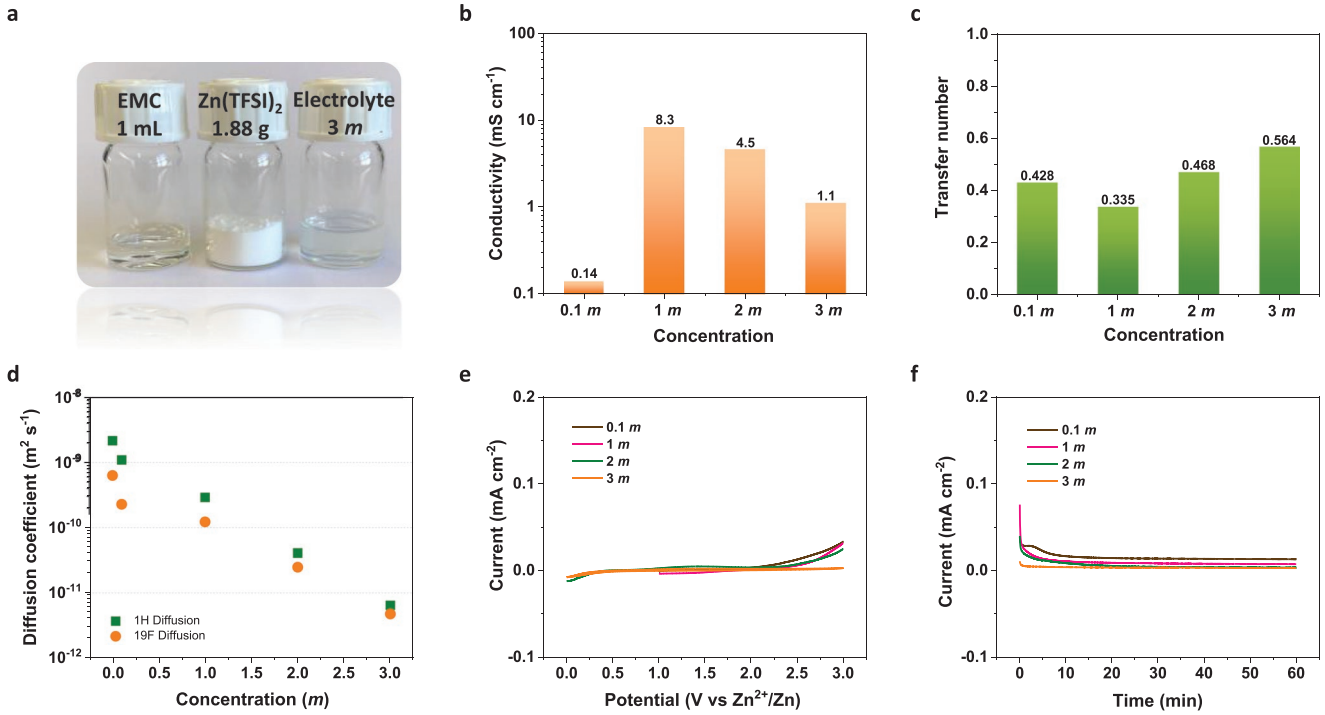

Figure 1. Property of $Zn(TFSI)_2$/EMC electrolyte. a) Optical photos of EMC solvent, $Zn(TFSI)_2$ and 3 *m* $Zn(TFSI)_2$/EMC electrolyte. b) Ionic conductivity and c) Zn^{2+} transfer number of $Zn(TFSI)_2$/EMC electrolytes. d) Diffusion coefficient of $TFSI^-$ as a function of concentration of $Zn(TFSI)_2$/EMC. e) LSV curves of $Zn(TFSI)_2$/EMC electrolyte on a W electrode under different concentrations. The scan rate is 5 mV s^{-1}. f) Floating test of different electrolytes on W electrode at 3 V.

it as a promising cathode substrate for our ZGB application. The electrochemical stability of $Zn(TFSI)_2$/EMC electrolyte on a W rod electrode was first investigated by linear sweep voltammetry (LSV) in a homemade Swagelok cell (Figure S2, Supporting Information). As shown in Figure 1e, the $Zn(TFSI)_2$/EMC electrolyte with a range of concentration of 0.1-3 *m*, all displays a wide electrochemical stability window over 3 V (vs Zn^{2+}/Zn) without noticeable anodic oxidation. The leak current at 3 V is 33 μA cm^{-2} for 0.1 *m* and only 3 μA cm^{-2} for 3 *m* electrolyte. In sharp contrast, when conventional stainless steel (SS) electrode was employed, the $Zn(TFSI)_2$/EMC electrolyte (≤2 *m*) showed obvious oxidation above 2 V (Figure S3a, Supporting Information). Only 3 *m* electrolyte could suppress the anodic current with a leak current of ≈50 μA cm^{-2}. A more aggressive floating test was then carried out at 3 V. The current of $Zn(TFSI)_2$/EMC electrolyte on the W electrode quickly falls close to 0 (Figure 1f), while the current of ≤2 *m* $Zn(TFSI)_2$/EMC on SS electrode fast goes up to 10 mA cm^{-2} and overflows (Figure S3b, Supporting Information), indicating severe anodic corrosion of $TFSI^-$. Even in the concentrated 3 *m* electrolyte, a high current of >0.8 mA cm^{-2} was identified on the SS electrode. Based on these results, W rather than SS is an ideal cathode substrate for $Zn(TFSI)_2$/EMC electrolytes without the anodic corrosion problem.

2.2. Zn Plating–Stripping Behavior

The anode substrate acts as the core of the "anode-free" ZGB concept, which needs to regulate uniform Zn deposition over the substrate in place of random growth as dendrite. Based on lessons learnt from Li-metal batteries, alloying reagents can be exploited as nucleation sites to direct the growth of Li metal.[16] Compared to Au and Pt, Ag is less expensive and easy to process. More importantly, Ag can form an alloy phase with Zn either at high temperatures (≈900 K)[17] or under electrochemical conditions.[18] We speculated that a thin Ag coating on the common Cu foil might facilitate Zn nucleation on the surface and guide Zn deposition. To verify our hypothesis, a strip of Ag coating with 40 nm in thickness and 1 mm in width was patterned onto Cu foil by photolithography (Figure S4, Supporting Information). As a quick screening, we conducted galvanostatic Zn deposition (0.02 mAh cm^{-2} at 0.2 mA cm^{-2}) in an open Zn cell with 1 *m* $ZnCl_2$ aqueous electrolyte. The energy-dispersive X-ray spectroscopy (EDX) mapping indicates that Zn was deposited preferentially on Ag coating over the Cu surface (**Figure 2**a and Figure S4, Supporting Information). The deposited Zn presents the same shape as Ag coating, implying the regulating role of Ag on Zn deposition.

To further examine the effectiveness of Ag coating in the organic electrolyte, we coated the whole surface of Cu foil with Ag (denoted as Cu–Ag). A 40 nm Ag coating changed the color of Cu foil from orange to shiny white (Figure S5a, Supporting Information), and the surface of Cu–Ag comprised numerous Ag nanoparticles (Figure S5b–d, Supporting Information). In a thickness of 40 nm, the Ag loading on Cu foil was estimated as only 42 μg cm^{-2}, which could be reduced further by technical optimization. The Zn deposition behavior on Cu–Ag and Cu foil was then compared in a Cu–Ag//Zn and a Cu//Zn cell

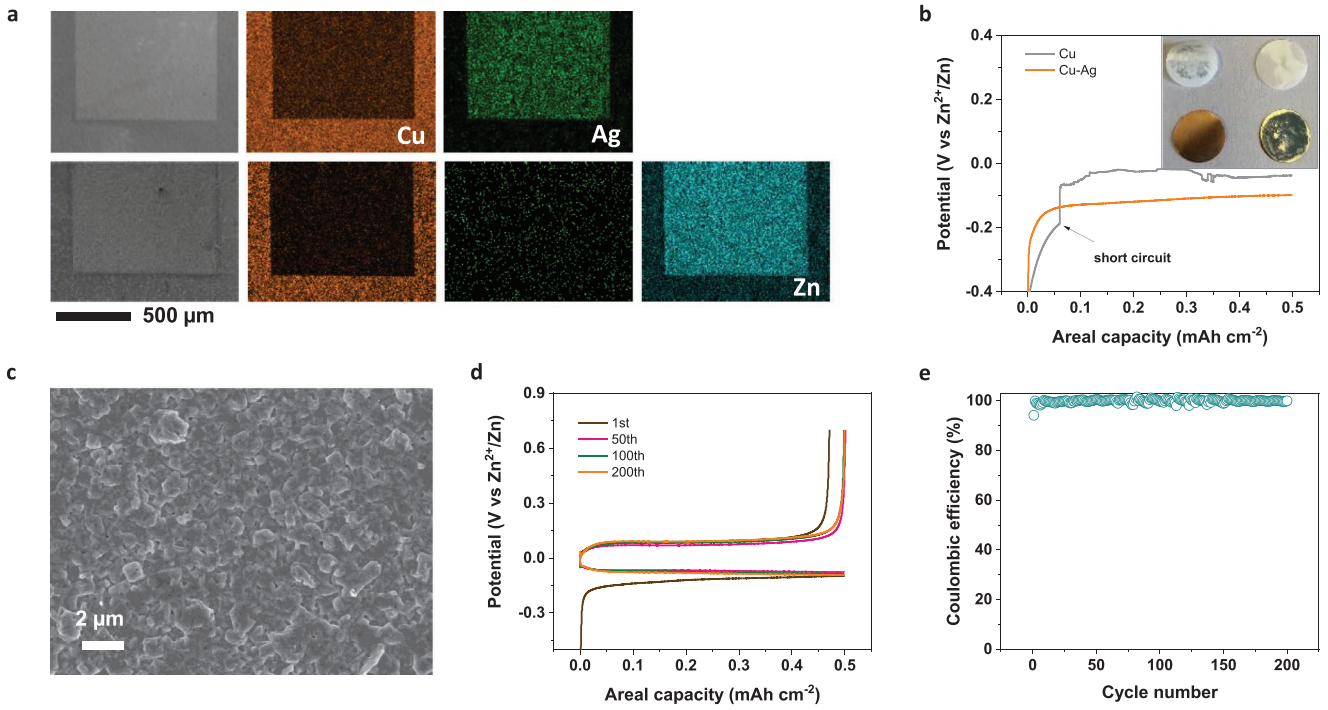

Figure 2. Zn deposition behavior on Ag-coated Cu. a) SEM images and EDX mapping of Ag-coated Cu before (top) and after (bottom) Zn deposition in 1 *m* $ZnCl_2$ aqueous electrolyte. The colored images show Cu as orange, Ag as green, and Zn as blue. b) The Zn deposition curve on bare Cu and Cu–Ag under a capacity of 0.5 mAh cm^{-2} at 0.5 mA cm^{-2}. The insets show optical photos of the separator and the electrode after the measurements. The electrolyte is 3 *m* $Zn(TFSI)_2$/EMC. c) SEM images of Zn deposited on Cu–Ag in 3 *m* $Zn(TFSI)_2$/EMC. d) Charge–discharge profiles of the Cu–Ag//Zn cell in 3 *m* $Zn(TFSI)_2$/EMC. The current density is 0.5 mA cm^{-2} and the capacity is 0.5 mAh cm^{-2}. e) The CE of Zn plating–stripping on Cu–Ag in 3 *m* $Zn(TFSI)_2$/EMC.

with 3 *m* $Zn(TFSI)_2$/EMC and Celgard 2400 used as the electrolyte and separator, respectively. On the bare Cu foil, a very small capacity (0.06 mAh cm^{-2}) of Zn deposition induced a short circuit of the cell (Figure 2b), which is attributed to the difficulty of Zn nucleation on Cu and subsequent vertical Zn growth through the separator. After the deposition, all deposited Zn was found located on the polypropylene separator instead of Cu foil. In contrast, when using Cu–Ag, no short circuit was detected under a deposition capacity of 0.5 mAh cm^{-2} or even 10 mAh cm^{-2} (Figure 2b; Figure S6, Supporting Information). The separator remained clean and intact after the deposition, while the deposited Zn was situated on the Cu–Ag. To explain the different Zn deposition behavior on Cu–Ag and Cu foil, the electric field distribution of the cross section of Cu–Ag and Cu were simulated by a finite element method.[18] The electric field distributed uniformly on Cu–Ag but concentrated on tips on Cu (Figure S7, Supporting Information), leading to uniform Zn deposition on Cu–Ag but off-plane Zn growth on Cu. Further cyclic voltammetry (CV) measurements of the Cu–Ag//Zn cell and the control Ag//Zn cell, as well as XRD analysis (Figures S8 and S9, Supporting Information) indicated that at the initial stage, Ag would be transformed into $AgZn/AgZn_3$ alloy, which functioned as zincophilic matter to guide the subsequent Zn metal deposition. Note that the initial high overpotential (>0.4 V) likely originates from Zn^{2+} diffusion through interphase formed on the fresh Zn anode[19] rather than from nucleation of Zn onto substrates because the high overpotential disappeared in the cell with a used Zn anode and a new Cu–Ag substrate (Figure S10, Supporting Information).

The morphology of the deposited Zn was surveyed by scanning electron microscopy (SEM) under different magnifications. In a wide field of vision, no dendrite was noticed (Figure S11, Supporting Information), and the deposited Zn existed in the form of closely packed micrometer-sized particles (Figure 2c). The plating–stripping efficiency of Zn on Cu–Ag was then evaluated by galvanostatic discharge-charge cycling under 0.5 mAh cm^{-2} at 0.5 mA cm^{-2}. The first stripping capacity reached 0.471 mAh cm^{-2}, corresponding to an initial CE of 94.2% (Figure 2d,e). From the second cycle, the CE climbed up to 99.90% and averaged 99.86% across 200 cycles. The overpotential of Zn plating–stripping on Cu–Ag was estimated as 205 mV for the initial cycle and 179 mV for the 200th cycle (Figure S12, Supporting Information). After cycling, some "dead Zn" was present on the Cu–Ag substrate (Figure S13, Supporting Information). Besides, high CE was achieved as well in 0.1, 1, and 2 *m* $Zn(TFSI)_2$/EMC (Figure S14, Supporting Information). A symmetric Zn//Zn cell showed excellent cycling performance without overpotential increase over 400 h (Figure S15, Supporting Information). However, it was found that Zn plating–stripping on Cu–Ag in 4 *m* $Zn(TFSI)_2$/EMC was difficult with large polarization and low CE (Figure S16b–e, Supporting Information).

2.3. Anion Intercalation into Graphite Cathode

To examine the electrochemical behavior of graphite cathode in $Zn(TFSI)_2$/EMC electrolyte, a conventional ZGB was

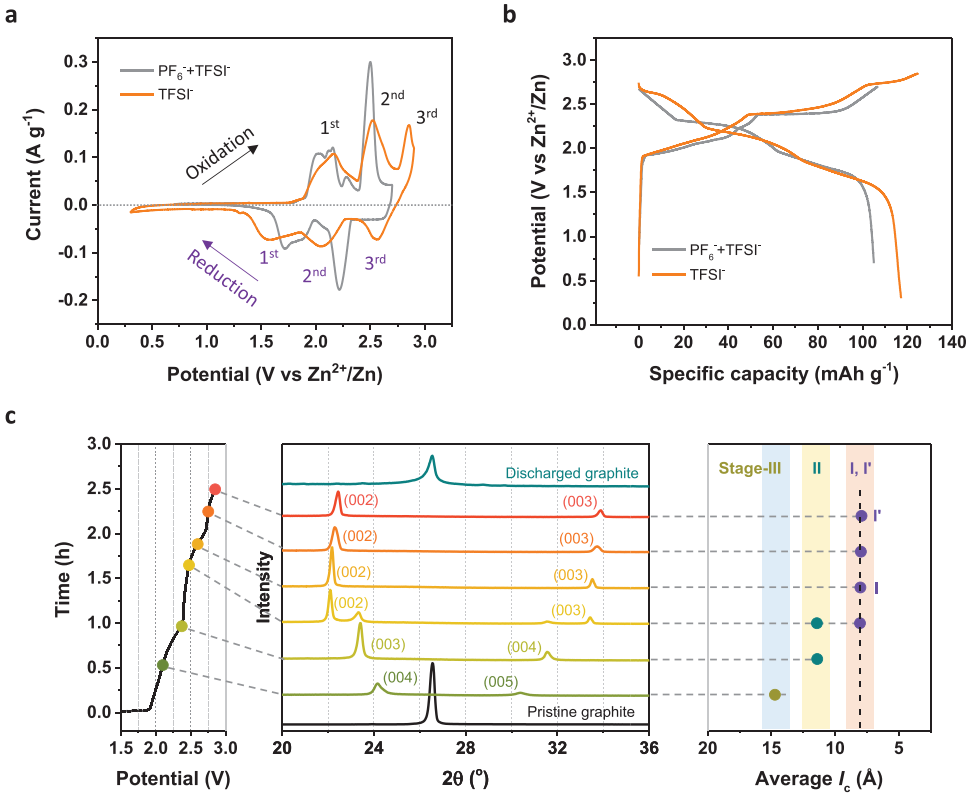

Figure 3. Electrochemical behavior of graphite cathode in 3 *m* $Zn(TFSI)_2$/EMC. a) CV curves comparison of graphite cathode with different anion intercalated. b) Corresponding charge–discharge profiles of graphite cathode with different anion intercalated. c) XRD analysis of graphite cathodes. Left: the galvanostatic charge curve. Middle: XRD patterns of graphite at different charging states. Right: periodic repeat distance (I_c) of $TFSI^-$-intercalated graphite.

constructed with a Zn foil anode and a commercial graphite cathode. $Zn(TFSI)_2$/EMC with a concentration over 3 *m* was avoided due to the trap of Zn^{2+} on the anode, which caused severe capacity fading of ZGB in short cycles (Figure S16f, Supporting Information). In a CV measurement, as shown in **Figure 3**a, the ZGB in 3 *m* $Zn(TFSI)_2$/EMC mainly showed three pairs of redox peaks in the voltage range of 0.30–2.85 V (vs Zn^{2+}/Zn), which derives from $TFSI^-$ intercalation (deintercalation) into (out of) graphite and does not influence by the cation used. A similar CV curve was obtained on graphite cathode in LiTFSI/EMC electrolyte except for a different working potential (Figure S17a, Supporting Information). The first and second oxidation peaks of graphite for pure $TFSI^-$ intercalation located at a similar potential to those for dual-anion (PF_6^-+$TFSI^-$) intercalation,[9a] while the first and second reduction peaks for $TFSI^-$ deintercalation downshifted by 0.1 V compared to those for dual-anion (PF_6^-+$TFSI^-$) deintercalation. The third pair of redox peaks at a high potential range (2.50–2.85 V) is exclusively observed during $TFSI^-$ intercalation–deintercalation, and absent for other anions like PF_6^- and FSI^- (Figure S17c, Supporting Information). These results manifest the existence of an additional graphite intercalation phase stabilized by $TFSI^-$ at room temperature, which is not identified for PF_6^- or FSI^-.

In agreement with CV results, the charge–discharge profiles of graphite cathode in $Zn(TFSI)_2$/EMC exhibited three charge plateaus (2.10 V, 2.40 V, and 2.75 V) and three discharge plateaus (1.75 V, 2.10 V, and 2.65 V), while two charge/discharge plateaus (2.10 V/1.85 V and 2.40 V/2.25 V) were noticed for the PF_6^-+$TFSI^-$ system (Figure 3b). Due to additional capacity contribution by the third charge plateau, the graphite cathode in $Zn(TFSI)_2$/EMC afforded a specific capacity of 117 mAh g^{-1}, over 10% higher than 105 mAh g^{-1} in dual-anion electrolyte[9a] and <100 mAh g^{-1} for PF_6^-[4d,20] and $AlCl_4^-$ intercalation.[3e,21] Further increasing the charge potential of graphite cathode in $Zn(TFSI)_2$/EMC to 2.90 V would induce an endless flat charging plateau, which stemmed from irreversible overcharge and contributed no additional discharge capacity (114 mAh g^{-1}; Figure S18, Supporting Information). The CE of graphite cathode at 0.3–2.85 V maintained 94–96% during cycling (Figure S19, Supporting Information). The ≈5% loss is probably related to the self-discharge behavior of graphite cathode at high potential, with electron/hole hopping between anode and cathode via EMC medium (Figure S20, Supporting Information).

To gain insight into the structural evolution of graphite cathode during charge, we conducted ex situ XRD measurements of graphite cathode at different charging states. The applied current density was 50 mA g^{-1}. Upon charging, the graphite (002) peak at 26.45° split into two new peaks at 22–25° and 30–35° (Figure 3c), which can be assigned as the (00*n*+1) and (00*n*+2) peaks of GICs. Based on the Bragg angles of (00*n*+1) and (00*n*+2) peaks, the structure parameters of $TFSI^-$-intercalated graphite can be calculated[22] (Table S1,

Supporting Information). The graphite cathode evolved to a Stage-III compound at 2.10 V and further transformed to Stage-II at 2.38 V and Stage-I at 2.60 V with a decreasing periodic repeat distance (I_c, Figure 3c). Both Stage-II and Stage-I phases were noticed at 2.44 V, which is indicative of a two-phase transformation at the charge plateau of 2.40 V. At 2.75 and 2.85 V, there were no other lower stages formed, but the I_c is even lower than that at 2.60 V (Table S1, Supporting Information), signifying that the transitions at the charge plateau of 2.75 V are solid solution[23] in nature and creating a Stage-I' phase at the end of charge. Based on the above results, the relation of stage information of graphite cathode with redox peaks can also be drawn, as shown in Figure S21 (Supporting Information). Normally, I_c decrease accompanied by sloping voltage curves was ascribed to closer packing of "rigid" anions (PF_6^-) inside graphite cathode, eliminating anion vibrations that expand the van der Waals gap of the anion containing the gallery.[24] Note that $TFSI^-$ is flexible in structure with two different conformational states (*trans* and *cis*),[25] and there is an equilibrium between $TFSI^-$ conformers in aprotic solvents.[26] The transoid form was found to be more stable than the cisoid form.[26] Similarly, our density functional theory (DFT) calculations suggest that the *trans*-$TFSI^-$-intercalated graphite is more stable by 0.435 eV than the *cis*-$TFSI^-$ intercalation compound (Figure S22, Supporting Information). Thus, we attribute the charge plateau at 2.75 V to *cis*-$TFSI^-$ intercalation into graphite and closer packing, because higher potential is necessary to reach the meta-stable intercalation phase.

2.4. Electrochemical Performance of the "Anode-Free" ZGB

Based on the above facts of highly reversible Zn plating–stripping on Cu–Ag and efficient $TFSI^-$ intercalation into graphite cathode, we thus constructed the first "anode-free" ZGB with Cu–Ag and graphite cathode in 3 *m* $Zn(TFSI)_2$/EMC electrolyte. The electrochemical performance of the "anode-free" ZGB was evaluated by galvanostatic cycling tests under 0.1–2.85 V. At the current density of 0.1 A g^{-1}, the cell delivered a specific capacity of 114 mAh g^{-1} based on graphite mass (2 mg cm^{-2}) in the cathode (**Figure 4**a). After 50 cycles, the specific capacity slightly faded to 110 mAh g^{-1}, corresponding to a capacity retention of 96.2%. The CE was determined as 94% for the initial cycle and stabilized ≈95% afterward. The typical charge–discharge curve of the "anode-free" ZGB resembled that of graphite cathode with three charge–discharge plateaus (Figure 4b).

Our "anode-free" ZGB with an average CE of 95% showed a superior cyclability to the "anode-free" rocking-chair metal-ion batteries under the same condition. It is predicted that an "anode-free" rocking-chair metal battery with a CE of 95% will lose over 50% of its capacity within 15 cycles.[12a] Such distinct cyclability difference points out the different inactivation paths between our "anode-free" ZGB and conventional "anode-free" rocking-chair metal batteries. In the latter case, a low CE means trap/loss of the only charge carrier due to a side reaction. Therefore, the cyclability was influenced by the CE as the exponent of a power law. In our case, the CE of the device did not suffer from trap/loss of Zn^{2+} or $TFSI^-$, but inherited from graphite cathode, likely caused by the self-discharge behavior at

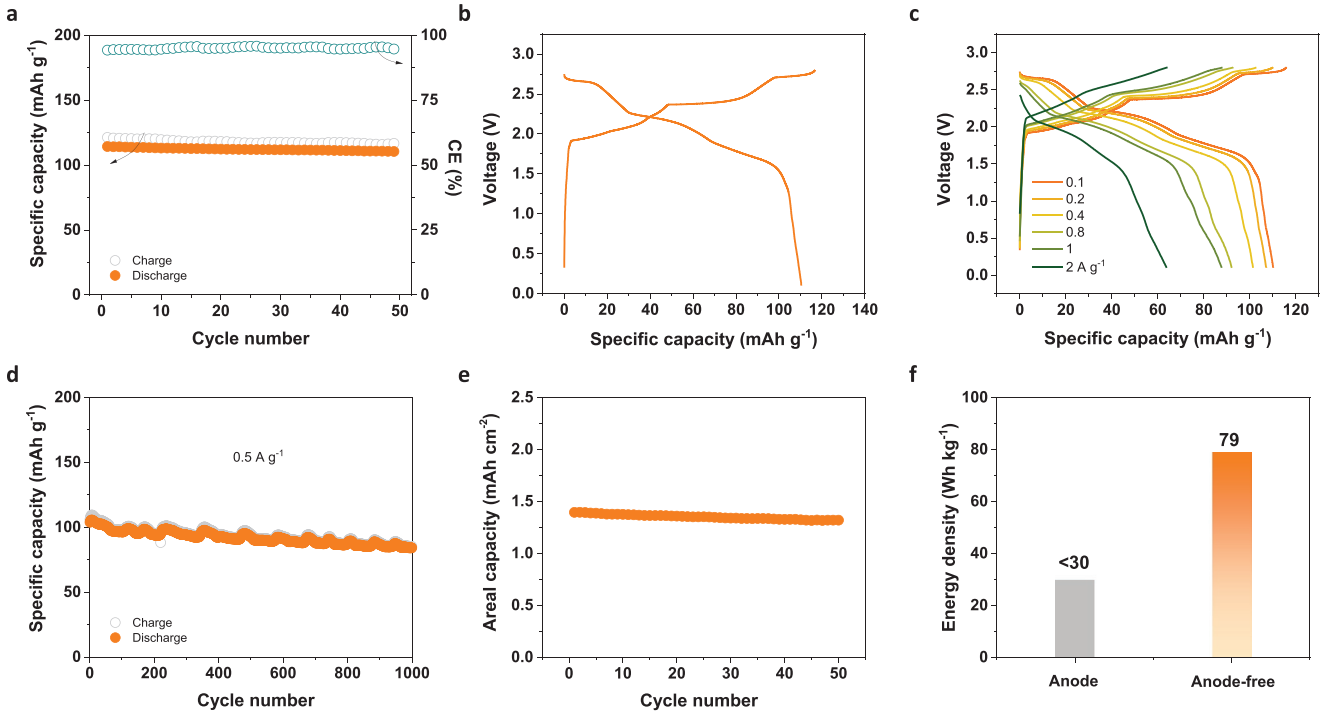

Figure 4. Electrochemical performance of anode-free ZGB. a) Cycling performance at 0.1 A g^{-1}. b) Typical charge–discharge curve of anode-free ZGB at 0.1 A g^{-1}. c) Rate performance at various current densities. d) Long-term cycling stability at 0.5 A g^{-1}. e) Cycling performance of anode-free ZGB with a graphite loading of 13 mg cm^{-2}. The current density and specific capacity of ZGB were calculated on graphite mass. f) Specific energy comparison of anode-free ZGB with other conventional ZGBs.

high potential. Therefore, the CE did not influence the cycling behavior.

The rate performance of the "anode-free" ZGB was investigated at various current rates ranging from 0.1 to 2 A g^{-1}. Polarization increased, especially for discharge branches, under accelerated current (Figure 4c). It seems that the discharge process (anion deintercalation-Zn stripping) is not as quick as the charging process (anion intercalation-Zn plating) of "anode-free" ZGB. Nevertheless, decent capacities of 88 and 64 mAh g^{-1} could be retained even at 1 and 2 A g^{-1}, respectively. The long-term cycling performance of the "anode-free" ZGB was assessed at 0.5 A g^{-1}. After 1000 galvanostatic cycles, the cell still retained a capacity of 84 mAh g^{-1}, corresponding to an impressive capacity retention of 82% in an "anode-free" configuration (Figure 4d; Figure S23, Supporting Information). It is worth noting that the repeated fluctuations in capacity came from changes in local temperature during the test. The areal capacity of the "anode-free" ZGB can be readily enhanced by increasing the areal mass loading of graphite cathode. Under loading of 13 mg cm^{-2}, the cell areal capacity reached 1.4 mAh cm^{-2} and remained stable during the cycling (Figure 4e; Figure S24, Supporting Information). Based on the total mass of graphite and electrolyte, the specific energy of our "anode-free" ZGB was estimated as 79 Wh kg^{-1}, which is much higher than <30 Wh kg^{-1} for conventional ZGBs (Figure 4f and Table S2, Supporting Information). Self-discharge of the "anode-free" ZGB remains to be suppressed, especially at high voltage (Figure S25, Supporting Information) and requires a systematical investigation in the future.

We also endeavored to expand the "anode-free" concept to Li deposition using the same Cu–Ag substrate. In a Cu–Ag//Li cell with 4 *m* LiFSI/EMC electrolyte, the discharge plateau at 0.06 V (vs Li^+/Li) corresponds to the formation of AgLi alloy.[27] Under 0.2 mAh cm^{-2} at 0.2 mA cm^{-2}, the Li plating–stripping on Cu–Ag affords a CE of 86.5% for the first cycle and 95.6% for the second cycle, which are much higher than 50% and <23% for the bare Cu foil (Figure S26, Supporting Information). The CE difference of Li plating–stripping indicates that Ag coating contributes to the high reversibility of Li deposition. However, from the third cycle, the CE of Li plating-–stripping on Cu–Ag deteriorates, which could be due to Li depletion by side reactions like unstable interphase. Other than anode substrate, electrolyte engineering is highly desired to passivate the reactive Li metal in the "anode-free" Li-based DIBs.

3. Conclusion

We have demonstrated the first "anode-free" ZGB by directing Zn deposition via Ag coating. Neither dendrite nor side reactions were involved in Zn plating–stripping cycles, resulting in 99.90% reversibility from the second cycle. An additional high-potential intercalation plateau was unraveled by intercalating $TFSI^-$ into the graphite cathode, providing a high capacity of 117 mAh g^{-1}. The constructed "anode-free" ZGB delivered a long-term cycling life over 1000 cycles with a capacity retention of 82% and high specific energy of 79 Wh kg^{-1}. Considering the advantages of "anode-free" battery configuration, such as low cost in warehousing, high safety, potential ambient assembly condition, and high energy density, further efforts are needed to develop cheap yet effective substrates, to solve the interphase issues and accomplish the "anode-free" battery concept in new battery systems.

Supporting Information

Supporting Information is available from the Wiley Online Library or from the author.

Acknowledgements

This work was financially supported by European Union's Horizon 2020 research and innovation program (GrapheneCore3 881603), SPE3 project funded by German Ministry for Education and Research (BMBF) under Forschung für neue Mikroelektronik (ForMikro) program, M-ERA.NET and Sächsisches Staatsministerium für Wissenschaft und Kunst (HYSUCAP 100478697), German Research Foundation (DFG) within the Cluster of Excellence, and CRC 1415 (Grant No. 417590517). The authors acknowledge the CFAED and the Dresden Center for Nanoanalysis (DCN) at TU Dresden. The authors acknowledge Dr. Xiaodong Li and Kui Chen for their support on finite element simulation. The authors gratefully acknowledge the GWK support for funding this project by providing computing time through the Center for Information Services and HPC (ZIH) at TU Dresden.

Open access funding enabled and organized by Projekt DEAL.

Conflict of Interest

The authors declare no conflict of interest.

Data Availability Statement

The data that support the findings of this study are available from the corresponding author upon reasonable request.

Keywords

anion intercalation, anode-free batteries, dual-ion batteries, plating–stripping, Zn batteries

Received: March 1, 2022
Revised: May 11, 2022
Published online: June 12, 2022

[1] a) I. A. Rodríguez-Pérez, *X. Ji, ACS Energy Lett.* **2017**, *2*, 1762; b) M. Wang, Y. Tang, *Adv. Energy Mater.* **2018**, *8*, 1703320; c) Q. Liu, Y. Wang, X. Yang, D. Zhou, X. Wang, P. Jaumaux, F. Kang, B. Li, X. Ji, G. Wang, *Chem* **2021**, *7*, 1993; d) G. J. Liang, F. N. Mo, X. L. Ji, C. Y. Zhi, *Nat. Rev. Mater.* **2021**, *6*, 109.

[2] Y. Li, Y. Lu, P. Adelhelm, M. M. Titirici, Y. S. Hu, *Chem. Soc. Rev.* **2019**, *48*, 4655.

[3] a) Y. Sui, C. Liu, R. C. Masse, Z. G. Neale, M. Atif, M. AlSalhi, G. Cao, *Energy Storage Mater.* **2020**, *25*, 1; b) J. Hao, X. Li, X. Song, Z. Guo, *EnergyChem* **2019**, *1*, 100004; c) T. Placke, A. Heckmann, R. Schmuch, P. Meister, K. Beltrop, M. Winter, *Joule* **2018**, *2*, 2528; d) G. Wang, M. Yu, X. Feng, *Chem. Soc. Rev.* **2021**, *50*, 2388;

e) M.-C. Lin, M. Gong, B. Lu, Y. Wu, D.-Y. Wang, M. Guan, M. Angell, C. Chen, J. Yang, B.-J. Hwang, H. Dai, *Nature* **2015**, *520*, 324; f) C. Yang, J. Chen, X. Ji, T. P. Pollard, X. Lü, C.-J. Sun, S. Hou, Q. Liu, C. Liu, T. Qing, Y. Wang, O. Borodin, Y. Ren, K. Xu, C. Wang, *Nature* **2019**, *569*, 245.

[4] a) S. Rothermel, P. Meister, G. Schmuelling, O. Fromm, H.-W. Meyer, S. Nowak, M. Winter, T. Placke, *Energy Environ. Sci.* **2014**, *7*, 3412; b) T. Placke, O. Fromm, S. F. Lux, P. Bieker, S. Rothermel, H.-W. Meyer, S. Passerini, M. Winter, *J. Electrochem. Soc.* **2012**, *159*, A1755; c) G. Wang, S. Oswald, M. Loffler, K. Mullen, X. Feng, *Adv. Mater.* **2019**, *31*, 1807712; d) G. Wang, F. Wang, P. Zhang, J. Zhang, T. Zhang, K. Mullen, X. Feng, *Adv. Mater.* **2018**, *30*, 1802949.

[5] a) M. Sheng, F. Zhang, B. Ji, X. Tong, Y. Tang, *Adv. Energy Mater.* **2017**, *7*, 1601963; b) X. Xu, K. Lin, D. Zhou, Q. Liu, X. Qin, S. Wang, S. He, F. Kang, B. Li, G. Wang, *Chem* **2020**, *6*, 902.

[6] K. V. Kravchyk, P. Bhauriyal, L. Piveteau, C. P. Guntlin, B. Pathak, M. V. Kovalenko, *Nat. Commun.* **2018**, *9*, 4469.

[7] X. Lei, Y. Zheng, F. Zhang, Y. Wang, Y. Tang, *Energy Storage Mater.* **2020**, *30*, 34.

[8] M. Wang, C. Jiang, S. Zhang, X. Song, Y. Tang, H. M. Cheng, *Nat. Chem.* **2018**, *10*, 667.

[9] a) G. Wang, B. Kohn, U. Scheler, F. Wang, S. Oswald, M. Loffler, D. Tan, P. Zhang, J. Zhang, X. Feng, *Adv. Mater.* **2020**, *32*, 1905681; b) P. Chen, J. Richter, G. Wang, D. Li, T. Pietsch, M. Ruck, *Small* **2021**, *17*, 2102058.

[10] a) Q. Guo, K.-I. Kim, S. Li, A. M. Scida, P. Yu, S. K. Sandstrom, L. Zhang, S. Sun, H. Jiang, Q. Ni, D. Yu, M. M. Lerner, H. Xia, X. Ji, *ACS Energy Lett.* **2021**, *6*, 459; b) X. Dong, H. Yu, Y. Ma, J. L. Bao, D. G. Truhlar, Y. Wang, Y. Xia, *Chem. - Eur. J.* **2017**, *23*, 2560; c) X. Wu, Y. Xu, C. Zhang, D. P. Leonard, A. Markir, J. Lu, X. Ji, *J. Am. Chem. Soc.* **2019**, *141*, 6338; d) Z. Huang, Y. Hou, T. Wang, Y. Zhao, G. Liang, X. Li, Y. Guo, Q. Yang, Z. Chen, Q. Li, L. Ma, J. Fan, C. Zhi, *Nat. Commun.* **2021**, *12*, 3106; e) J. M. Wrogemann, S. Künne, A. Heckmann, I. A. Rodríguez-Pérez, V. Siozios, B. Yan, J. Li, M. Winter, K. Beltrop, T. Placke, *Adv. Energy Mater.* **2020**, *10*, 1902709.

[11] X. Tong, X. Ou, N. Wu, H. Wang, J. Li, Y. Tang, *Adv. Energy Mater.* **2021**, *11*, 2100151.

[12] a) S. Nanda, A. Gupta, A. Manthiram, *Adv. Energy Mater.* **2021**, *11*, 2000804; b) R. Weber, M. Genovese, A. J. Louli, S. Hames, C. Martin, I. G. Hill, *J. R. Dahn, Nat. Energy* **2019**, *4*, 683; c) A. J. Louli, A. Eldesoky, R. Weber, M. Genovese, M. Coon, J. deGooyer, Z. Deng, R. T. White, J. Lee, T. Rodgers, R. Petibon, S. Hy, S. J. H. Cheng, *J. R. Dahn, Nat. Energy* **2020**, *5*, 693.

[13] A. P. Cohn, N. Muralidharan, R. Carter, K. Share, C. L. Pint, *Nano Lett.* **2017**, *17*, 1296.

[14] a) Y. Zhu, Y. Cui, H. N. Alshareef, *Nano Lett.* **2021**, *21*, 1446; b) F. Ming, Y. Zhu, G. Huang, A. H. Emwas, H. Liang, Y. Cui, H. N. Alshareef, *J. Am. Chem. Soc.* **2022**, *144*, 7160.

[15] a) S. Wang, K. V. Kravchyk, A. N. Filippin, U. Müller, A. N. Tiwari, S. Buecheler, M. I. Bodnarchuk, M. V. Kovalenko, *Adv. Sci.* **2018**, *5*, 1700712; b) G. Wang, E. Dmitrieva, B. Kohn, U. Scheler, Y. Liu, V. Tkachova, L. Yang, Y. Fu, J. Ma, P. Zhang, F. Wang, J. Ge, X. Feng, *Angew. Chem., Int. Ed.* **2022**, *61*, 202116194.

[16] a) C. Yang, Y. Yao, S. He, H. Xie, E. Hitz, L. Hu, *Adv. Mater.* **2017**, *29*, 1702714; b) Y.-G. Lee, S. Fujiki, C. Jung, N. Suzuki, N. Yashiro, R. Omoda, D.-S. Ko, T. Shiratsuchi, T. Sugimoto, S. Ryu, J. H. Ku, T. Watanabe, Y. Park, Y. Aihara, D. Im, I. T. Han, *Nat. Energy* **2020**, *5*, 299; c) K. Yan, Z. Lu, H.-W. Lee, F. Xiong, P.-C. Hsu, Y. Li, J. Zhao, S. Chu, Y. Cui, *Nat. Energy* **2016**, *1*, 16010.

[17] a) T. Hatsukade, K. P. Kuhl, E. R. Cave, D. N. Abram, J. T. Feaster, A. L. Jongerius, C. Hahn, T. F. Jaramillo, *Energy Technol.* **2017**, *5*, 955; b) Y. Xie, L. Zhao, Z. Zhang, X. Wang, R. Wang, C. Cui, *Mater. Chem. Phys.* **2018**, *219*, 433; c) Y. Matsuo, T. Suzuki, A. Nagasawa, *J. Phys. Soc. Jpn.* **1980**, *49*, 1344.

[18] T. Chen, Y. Wang, Y. Yang, F. Huang, M. Zhu, B. T. W. Ang, J. M. Xue, *Adv. Funct. Mater.* **2021**, *31*, 2101607.

[19] L. Cao, D. Li, T. Pollard, T. Deng, B. Zhang, C. Yang, L. Chen, J. Vatamanu, E. Hu, M. J. Hourwitz, L. Ma, M. Ding, Q. Li, S. Hou, K. Gaskell, J. T. Fourkas, X. Q. Yang, K. Xu, O. Borodin, C. Wang, *Nat. Nanotechnol.* **2021**, *16*, 902.

[20] G. Wang, M. Yu, J. Wang, D. Li, D. Tan, M. Loffler, X. Zhuang, K. Mullen, X. Feng, *Adv. Mater.* **2018**, *30*, 1800533.

[21] a) C.-J. Pan, C. Yuan, G. Zhu, Q. Zhang, C.-J. Huang, M.-C. Lin, M. Angell, B.-J. Hwang, P. Kaghazchi, H. Dai, *Proc. Natl. Acad. Sci. U.S.A.* **2018**, *115*, 5670; b) M. Angell, C.-J. Pan, Y. Rong, C. Yuan, M.-C. Lin, B.-J. Hwang, H. Dai, *Proc. Natl. Acad. Sci. U.S.A.* **2017**, *114*, 834.

[22] a) G. Schmuelling, T. Placke, R. Kloepsch, O. Fromm, H.-W. Meyer, S. Passerini, M. Winter, *J. Power Sources* **2013**, *239*, 563; b) T. Placke, G. Schmuelling, R. Kloepsch, P. Meister, O. Fromm, P. Hilbig, H.-W. Meyer, M. Winter, *Z. Anorg. Allg. Chem.* **2014**, *640*, 1996.

[23] J. A. Read, *J. Phys. Chem. C* **2015**, *119*, 8438.

[24] J. A. Seel, J. R. Dahn, *J. Electrochem. Soc.* **2000**, *147*, 892.

[25] a) P. Johansson, S. P. Gejji, J. Tegenfeldt, J. Lindgren, *Electrochim. Acta* **1998**, *43*, 1375; b) K. Fujii, T. Fujimori, T. Takamuku, R. Kanzaki, Y. Umebayashi, S.-i. Ishiguro, *J. Phys. Chem. B* **2006**, *110*, 8179.

[26] M. Herstedt, M. Smirnov, P. Johansson, M. Chami, J. Grondin, L. Servant, J. C. Lassègues, *J. Raman Spectrosc.* **2005**, *36*, 762.

[27] S. Jin, Y. Ye, Y. Niu, Y. Xu, H. Jin, J. Wang, Z. Sun, A. Cao, X. Wu, Y. Luo, H. Ji, L.-J. Wan, *J. Am. Chem. Soc.* **2020**, *142*, 8818.